INTERNATIONAL JOURNAL FOR NUMERICAL METHODS IN FLUIDS
Int. J. Numer. Meth. Fluids 2009; **60**:1079–1102
Published online 24 September 2008 in Wiley InterScience (www.interscience.wiley.com). DOI: 10.1002/fld.1922

Robust design and numerical simulation on drag reduction by a mixture film for liquid turbulence in a channel

Sheng-Ju Wu[1,*,†], Kwan Ouyang[2] and Sheau-Wen Shiah[1]

[1]*Department of Power Vehicle and Systems Engineering, Chung Cheng Institute of Technology, National Defense University, Taoyuan, Taiwan*
[2]*Graduate School of Defense Science, Chung Cheng Institute of Technology, National Defense University, Taoyuan, Taiwan*

SUMMARY

An important way of increasing the speed and lowering the fuel consumption of ships is by decreasing the frictional drag. One of the most promising techniques for reducing drag is the use of air bubbles. The goal of this investigation is to establish a set of optimum robust parametric levels for drag reduction by a mixture (air–water) film in turbulent channel flow. Based on the conditions laid out by the Taguchi orthogonal array method, turbulent flows, with air bubbles injected into a channel, are simulated using commercial computational fluid dynamics software. The local shear stress on the upper wall is computed to evaluate the efficiency of drag reduction. Many factors can affect drag reduction. The factors investigated in this study are the rate of air injection, bubble size, area of air injection, flow speed, and measured position of the shear stress. These factors have been investigated through the analysis of variance, which has revealed that the rate of air injection and water flow speed dominate the efficiency of drag reduction by a mixture film. According to the results, the drag can be reduced by an average of 83.4%; and when the configuration of the parametric levels is optimum the maximum drag reduction of 88.5% is achieved.

Received 14 February 2008; Revised 6 August 2008; Accepted 8 August 2008

KEY WORDS: mixture film; drag reduction; Taguchi method; robust design; numerical simulation; finite volume methods

1. INTRODUCTION

Increasing speed and lowering fuel consumption for ships have always been major issues for naval architects. When moving forward, the main drag that a vessel encounters underwater is frictional resistance. If this resistance is reduced, the speed of the vessel will increase and the

*Correspondence to: Sheng-Ju Wu, Department of Power Vehicle and Systems Engineering, Chung Cheng Institute of Technology, National Defense University, No. 190, Sanyuan 1st St., Ta-Hsi, Taoyuan 335, Taiwan.
†E-mail: wusj@ndu.edu.tw, wusj44@yahoo.com.tw

fuel consumption will be reduced. Various techniques have been proposed for the reduction of frictional resistance. One such method is the use of bubbles, which has drawn widespread interest because it has shown significant efficiency in drag reduction, is easy to implement, and has no adverse effect on the environment. There are two main approaches for the utilization of bubbles, which vary according to the bubble size generated. One is called 'microbubble drag reduction', and it utilizes small bubbles that are dispersed into the liquid turbulent boundary layer in an effort to curtail the Reynolds stress. The other technique is to cover the material body with a large film of air, in order to separate the material surface from the water, thus reducing drag. The use of an air film reduces friction more than the use of microbubbles; however, the maintenance of an air film is difficult. Under high-speed operation, an air film only provides substantial frictional reduction near the point of air injection.

The application of microbubbles for drag reduction was first used by McCormick and Bhattacharyya [1], who used electrolysis to generate microbubbles and distribute them in the boundary layer of a moving submerged vessel. Their findings show that microbubbles effectively reduce frictional resistance. Since then, most scholars have generated microbubbles by pushing compressed air through a porous medium, in order to improve the generation of microbubbles. The reduction of frictional resistance in a liquid turbulent flow through the use of microbubbles arises for two reasons. First, the use of microbubbles lowers the average viscosity and density of the gas–liquid mixture flow and second, it suppresses the Reynolds stress through the interaction of microbubbles with the liquid [2]. However, the mechanism of drag reduction has not yet been firmly established.

Many instruments have been used to investigate the mechanism of drag reduction due to microbubbles in the turbulent boundary layer. For example, Dubnishchev *et al.* [3] used a laser Doppler velocimeter (LDV) and a thermal film velocimeter to measure the bubble volume concentrations and velocity profiles. The outcome of the experiment showed that the bubble concentration in the viscous sublayer was zero and the maximum concentration was measured at $\bar{y} = y/2H = 0.1$, where y denotes the distance from the wall and H denotes the vertical height of the test section. In studying the interaction of microbubbles with a liquid turbulent boundary layer, Merkle and Deutsch [4] concluded that microbubbles have to spread within the buffer layer and act in a polymer-like manner to reduce the frictional resistance. Kato *et al.* [5] employed an LDV to measure the time histories of average flow speeds and turbulent intensities when bubbles were injected into the turbulent boundary layer. Kawamura *et al.* [6] utilized cavitation to generate bubbles and examined the effect of bubble size on the efficiency and sustainability of drag reduction.

In the internal flow, microbubbles are capable of significantly reducing frictional resistance. For example, Madavan *et al.* [7] conducted an experiment on microbubble drag reduction between two flat plates and achieved an 80% reduction in drag. In the Kato *et al.* experiment [5], the highest reduction efficiency achieved was 60%. Tsai and Chen [8] measured the total resistance drag of flat plate in water tunnel as well as in towing tank; results showed that maximum drag reduction by the microbubbles was about 80% at water tunnel. However, in real-world applications, when this reduction technique is employed on a full-scale vessel, it is difficult to ensure that the bubbles remain within the boundary layer due to their buoyancy, and as a result, the reduction efficiency drops greatly. Latorre [9] utilized the microbubble drag reduction technique on both small-scale models and full-scale ships; the efficiencies of drag reduction were 10–12 and 15–18% for the model ships and full-scale ships, respectively. In the full-scale ship experiments conducted by Kato and Kodama [10], the authors operated an underwater TV camera and observed that the bubbles did not spread thinly over the ship's hull, and instead formed likely chimney smoke downstream. Furthermore, when bubbles were injected, the effective density of flow into the propeller was

DOI: 10.1002/fld

reduced by the air bubbles, reducing the efficiency of propeller performance by 3–6%. Latorre *et al.* [11] used both microbubbles and surface coating to reduce the drag for a 2.3 m model ship, but the reduction efficiency was only 4–11%.

Some of the drag reduction studies listed above utilize relatively large bubbles compared with the boundary layer thickness; however, these authors will still often use the term 'microbubbles' as a keyword, because the bubble size is surely smaller than the effective length of the drag reduction area. These two methods (the microbubble and air film methods) have been investigated separately, but the intermediate condition that occurs in the transition between microbubbles and air film has not been investigated thoroughly. Hence, Murai *et al.* [12] studied the drag reduction at the intermediate bubble size condition, which occurs between the microbubble and air film states. The bubble sizes used in that experiment were in the range of 2–90 mm. It was determined that the local shear stress substantially decreases at the rear of the individual large bubbles, while the front region exhibits a slight increase.

Many numerical studies have attempted to elucidate the interaction between a liquid turbulent boundary layer and bubbles. Among these studies, some have utilized direct numerical simulation (DNS) (e.g. Kawamura and Kodama [13, 14] and Sugiyama *et al.* [15]). DNS procedures are used to directly resolve the Navier–Stokes equation and to treat the gas–liquid interface using a free surface condition. However, the DNS capacity of current computers is limited. They are only capable of simulating a flow containing several hundred bubbles and, thus, are incapable of accurately simulating a real situation, which would involve a substantially larger number of bubbles. Additionally, some researchers have used the two-fluid model (e.g. Drew [16]; Murai and Matsumoto [17]), while others have created a simple model employing two phases to simulate the interaction between the bubbles and the liquid turbulent flow (e.g. Legner [18], Madavan *et al.* [19] and Marie [20]).

This study pays much attention to the determination of optimum robust parametric levels of drag reduction, instead of the presentation of the flow pattern. Many factors affect bubble drag reduction; this study investigates some critical factors, which include the following: the rate of air injection, the area of air injection, bubble size, flow speed, and the measured position of the shear stress on wall. Various values of shear stress measured at different positions can be used to examine the sustaining efficiency of bubbles in drag reduction. The researches mentioned above have predominantly paid attention to only one factor at a time when investigating the effect of bubbles and have, therefore, all suffered from the same limitation, that they are unable to investigate the interaction between different factors. Hence, predicting the optimum conditions for factorial parametric levels in bubble drag reduction has not yet been rigorously investigated. The implementation of the design of experiment methodology to plan experimental conditions can be utilized to systematically assess the effects of parametric levels on the response. The application of robust parametric design allows determination of the optimal factorial parametric level of quality by taking into account the fact that quality may be affected by the manufacture and production, as well as disturbance from the environment. The controllable factors are the factors that may have their parametric levels set by the technique, and the selection of these levels should have some significance to the experiment. Therefore, the rate of air injection, the area of air injection, and the bubble size are treated as controllable factors in this study. However, if this technique is used to set the parametric level of a factor but the resulting level is not meaningful, then the factor is referred to as an indicative factor. The effect of an indicative factor on the response can be considered as variance due to the external environment. Although the flow speed and measured position of shear stress can be easily arranged in the experiment, their manipulation has no meaning. Hence, in this

DOI: 10.1002/fld

investigation, the various flow speeds and measured positions of shear stress are considered as indicative factors. For a robust parametric design, the Taguchi orthogonal array method [21, 22] is usually adopted to plan a minimum number of experiments and to determine the experimental condition that has the least variability as the optimum robust condition. When using the Taguchi method, a fractional–factorial experiment is often used instead of a full-factorial experiment, in order to lower the cost and time of an investigation while maintaining credible results. The Taguchi method has been widely adopted in industry and applied in various applications. For example, Kim *et al.* [23] used the Taguchi method to evaluate the effect of several factors on particle size and size distribution for the synthesis of zinc oxide (ZnO), and obtained ZnO nanoparticles (about 30 nm) under optimal conditions. Using the Taguchi method, Nikbakht *et al.* [24] investigated the effect of operating parameters on the concentration of citric acid in an effort to improve the performance of an electrodialysis system.

Following significant advances in computer mathematical processing power, maturation of various numerical models and demand for increased understanding of the complexity in physical phenomena and geometrical formations, commercial computational fluid dynamics software has usually been employed to simulate the complicated flow. FLUENT is a commercial software package commonly used in the field of fluid dynamics. It utilizes the control-volume method to resolve the flow field and offers various numerical models that are useful for a wide range of applications. This study initially established its experimental conditions based on the orthogonal array supplied by Dr Taguchi and used FLUENT to resolve the two-phase flow with bubbles, and to seek a set of optimum robust parametric levels for drag reduction. In addition, analysis of variance (ANOVA) is employed to investigate the effect of factors and their interactions on drag reduction.

2. NUMERICAL METHOD

2.1. Problem description

Figure 1 represents a schematic diagram of the numerical channel. As the flow enters the channel, it has been fully developed. Downstream of the left inlet of the channel, porous media of various sizes are installed on the upper wall. Compressed air passes through a porous medium to form air bubbles that are injected into the flow. The gas–liquid mixture flows out through the outlet on the right. Three sizes of porous media are studied in this paper; the lengths of the streamwise (x-coordinate) and the lateral direction (z-coordinate) are 30 mm × 100 mm, 60 mm × 100 mm, and 90 mm × 100 mm, respectively. For the channel simulated in this study, the width and the height (y-coordinate) are 150 and 15 mm, respectively. The distance from the left edge of the porous medium to the left inlet of the channel is 300 mm. The distance from the right outlet of the channel

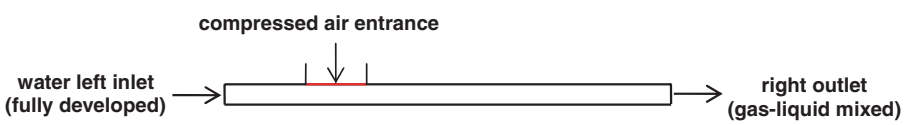

Figure 1. Schematic diagram of numerical channel.

DOI: 10.1002/fld

to the right edge of the porous medium is 500 mm. Consequently, the total length of the channel varies according to the size of the porous medium.

In order to obtain complete data on a fully developed turbulent flow, the single-phase flow without bubbles is resolved first and then the velocity profile and turbulent parameters are recorded at a given distance downstream of the entrance length. The local shear stresses obtained by the single-phase flow are also recorded to facilitate comparison with the local shear stresses of bubble flows, in order to evaluate the efficiency of drag reduction. As the two-phase flow is simulated, the velocity profile and turbulence parameters obtained from the single-phase flow serve as the boundary conditions of the left inlet of the channel, and the air bubbles are injected into the flow from the upper wall.

2.2. Basic assumptions of the numerical simulation

Physically, even though the field possesses a two-dimensional flow, the structure of the turbulence always transports in three dimensions. Hence, this study simulated turbulent channel flow in three dimensions. The two-phase flow with bubbles is assumed to be incompressible in this study, because the volumetric change of the bubbles in the turbulent boundary layer is taken as a secondary factor, based on the reasoning that bubbles can reach a balance between the interface of gas and liquid. To summarize, the basic assumptions of the numerical simulation in this study are: (1) the flow is an incompressible, steady, turbulent flow; (2) the primary flow is water in a continuous phase and its density and dynamic viscosity are constant; (3) the bubbles are generated by air in a dispersed phase and its density and dynamic viscosity are constant; (4) the bubble size is constant as bubbles spread downstream; (5) in considering buoyancy, the gravitational acceleration is set at $9.81\,\mathrm{m/s^2}$ downward; and (6) the thermal effect is neglected.

2.3. The governing equations and the turbulent model

The governing equations used to resolve the two-phase turbulent flow are a continuity equation and a momentum equation along with the turbulent model and two-phase model. Based on the assumption of a steady flow, the continuity equation is as follows:

$$\nabla \cdot (\rho \mathbf{V}) = 0 \tag{1}$$

where ρ represents the density and $\mathbf{V}$ is the velocity vector. The momentum equation is as follows:

$$\nabla \cdot (\rho \mathbf{V}\mathbf{V}) = -\nabla p + \nabla \cdot (\overline{\tau}) + \rho \mathbf{g} + \mathbf{F} \tag{2}$$

where p is static pressure, $\rho\mathbf{g}$ is the gravitational term, $\mathbf{F}$ is the body force , and $\overline{\tau}$ the stress tensor, can be obtained from the following:

$$\overline{\tau} = \mu[(\nabla \mathbf{V} + \nabla \mathbf{V}^{\mathrm{T}}) - \tfrac{2}{3}\nabla \cdot \mathbf{V} I] \tag{3}$$

μ is the molecular viscous coefficient and I is the unit tensor. The second term on the right-hand side of Equation (3) represents the effect of dilation. Details on this term can be examined in the FLUENT user's guide [25].

FLUENT provides various turbulent models; the widely applicable standard k–ε turbulent model is adopted in this paper. In the standard k–ε turbulent model, the transport equation for the turbulent

DOI: 10.1002/fld

kinetic energy per unit mass (k) and its dissipation rate (ε) are resolved as follows:

$$\rho u_i \frac{\partial \kappa}{\partial x_i} = \frac{\partial}{\partial x_i}\left[\left(\mu + \frac{\mu_t}{\sigma_\kappa}\right)\frac{\partial \kappa}{\partial x_i}\right] + G_\kappa + G_b - \rho\varepsilon \tag{4}$$

$$\rho u_i \frac{\partial \varepsilon}{\partial x_i} = \frac{\partial}{\partial x_i}\left[\left(\mu + \frac{\mu_t}{\sigma_\varepsilon}\right)\frac{\partial \varepsilon}{\partial x_i}\right] + C_{1\varepsilon}\frac{\varepsilon}{\kappa}(G_\kappa + G_{3\varepsilon}) - C_{2\varepsilon}\rho\frac{\varepsilon^2}{\kappa} \tag{5}$$

The details of the derivations for Equations (4) and (5) are demonstrated in Versteeg and Malalasekera [26].

2.4. Multi-phase model

FLUENT provides four models to handle multi-phase flows. Three of these are based on the Euler–Euler approach, while the fourth is based on the Euler–Lagrange approach. For the multi-phase flow with bubbles, FLUENT recommends the application of the Eulerian model or the Mixture model, which are both based on the Euler–Euler approach. In these two models, the phases are treated mathematically as interpenetrating continua. The Eulerian model solves a set of n momentum and continuity equations, while the Mixture model solves the mixture momentum and continuity equations and prescribes relative velocities to describe the dispersed phases. Theoretically, the Eulerian model produces results that are more precise, but its large requirements for computer memory and its poor numerical convergence are its weak points. To ensure precise shear stress on the wall of the turbulent flow, the mesh in the boundary layer must be very fine, which means that a large amount of computer memory is needed for the computation. Considering the limitations of computer hardware, this study adopts the Mixture model. The Mixture model regards multi-phase flow as a single mixture flow by establishing the volume fractions of each phase and the slip velocities among each phase to describe the dispersed phases. In the Mixture model, the main flow is set as a primary phase and regarded as the continuous phase; other phases are set as secondary phases and regarded as the dispersed phases. The Mixture model solves the continuity and momentum equations for the mixture, and volume fraction equations and relative velocities (to the primary phase) for the dispersed phases.

(1) The continuity equation for the mixture is

$$\nabla \cdot (\rho_{\mathrm{m}} \mathbf{V}_{\mathrm{m}}) = 0 \tag{6}$$

where ρ_{m} and $\mathbf{V}_{\mathrm{m}}$ are the density and velocity of the mixture, respectively, and $\mathbf{V}_{\mathrm{m}}$ can be expressed as

$$\mathbf{V}_{\mathrm{m}} = \frac{\sum_{k=1}^{n} \alpha_k \rho_k \mathbf{V}_k}{\rho_{\mathrm{m}}} \tag{7}$$

where α_k and ρ_k are the volume fraction and density of phase k, n is the total number of phases; $\mathbf{V}_k$ in Equation (7) represents the velocity of phase k.

(2) The momentum equation for the mixture is

$$\nabla \cdot (\rho_{\mathrm{m}} \mathbf{V}_{\mathrm{m}} \mathbf{V}_{\mathrm{m}}) = -\nabla p + \nabla \cdot [\mu_{\mathrm{m}} (\nabla \mathbf{V}_{\mathrm{m}} + \nabla \mathbf{V}_{\mathrm{m}}^{\mathrm{T}})] + \rho_{\mathrm{m}} \mathbf{g} + \mathbf{F} + \nabla \cdot \left(\sum_{k=1}^{n} \alpha_k \rho_k \mathbf{V}_{\mathrm{dr},k} \mathbf{V}_{\mathrm{dr},k} \right) \tag{8}$$

DOI: 10.1002/fld

where μ_{m} is the dynamic viscous coefficient of the mixture, $\mathbf{V}_{\mathrm{dr},k}$ is the drift velocity of phase k and is defined as

$$\mathbf{V}_{\mathrm{dr},k} = \mathbf{V}_k - \mathbf{V}_{\mathrm{m}} \tag{9}$$

For the primary phase q and dispersed phase p, the drift velocity and the relative velocity ($\mathbf{V}_{qp}$) are connected by the following expression:

$$\mathbf{V}_{\mathrm{dr},p} = \mathbf{V}_{pq} - \sum_{k=1}^{n} c_k \mathbf{V}_{qk} \tag{10}$$

where the c_k represents the mass fraction and is defined as $c_k = \alpha_k \rho_k / \rho_{\mathrm{m}}$.

(3) The relative velocity of the dispersed phase to the primary phase is

For $\mathbf{V}_{pq}$, which represents the relative velocity of the dispersed phase (p) relative to the primary phase (q), FLUENT adopts the formulation provided by Maaninen *et al.* (1966):

$$\mathbf{V}_{pq} = \frac{\tau_{\mathrm{p}}}{f_{\mathrm{drag}}} \frac{(\rho_p - \rho_{\mathrm{m}})}{\rho_p} \mathbf{a} - \frac{v_m}{\alpha_p \sigma_D} \nabla \alpha_q \tag{11}$$

where τ_{p} is the particle relaxation time written as

$$\tau_{\mathrm{p}} = \frac{\rho_p d^2}{18 \mu_q} \tag{12}$$

d is the diameter of the bubble and $\mathbf{a}$ in Equation (11) is the acceleration of the bubble:

$$\mathbf{a} = \mathbf{g} - (\mathbf{V}_{\mathrm{m}} \cdot \nabla) \mathbf{V}_{\mathrm{m}} - \frac{\partial \mathbf{V}_{\mathrm{m}}}{\partial t} \tag{13}$$

With regard to the drag function, f_{drag}, FLUENT provides various formulations. This study adopts the default option developed by Schiller and Naumann in 1995:

$$f_{\mathrm{drag}} = \begin{cases} 1 + 0.15 Re^{0.687} & Re \leqslant 1000 \\ 0.0183 Re & Re > 1000 \end{cases} \tag{14}$$

Re represents the relative Reynolds number. The relative Reynolds number for the primary phase q and dispersed phase p is obtained as

$$Re = \frac{\rho_q |\mathbf{V}_p - \mathbf{V}_q| d}{\mu_q} \tag{15}$$

(4) Equation of volume fraction for dispersed phases:

If the mass transfer between phases is not taken into account, the volume fraction of the dispersed phase (p) can be obtained from the following equation:

$$\nabla \cdot (\alpha_p \rho_p \mathbf{V}_{\mathrm{m}}) = -\nabla \cdot (\alpha_p \rho_p \mathbf{V}_{\mathrm{dr},p}) \tag{16}$$

DOI: 10.1002/fld

2.5. Boundary conditions

Referring to Figure 1, the numerical channel has three inlet and outlet boundaries: the left inlet (water entrance), the inlet on upper wall (air injection), and the right outlet (gas–liquid flow exit). The boundary condition of the left inlet is set up as a 'velocity inlet condition'. This indicates that the velocity profile and turbulent parameters obtained by the fully developed single-phase flow are used as the boundary condition for the water, and the volume fraction of water is set to one. In addition, both the velocity and volume fraction for air are set to zero. For the boundary condition of the inlet on the upper wall, the 'velocity inlet condition' is again adopted. The velocity and volume fraction for water are set to zero; for air, the y-component of velocity can be established by the rate of air injection and area of air injection, and the volume fraction is set to one. The right outlet boundary condition is set with the 'pressure outlet condition'. This indicates that the gradients of flow properties in the streamwise direction are equal to zero. All walls of the channel are assumed to have a no slip condition.

3. DESIGN OF THE EXPERIMENTAL CONDITIONS

The controllable factors related to bubble drag reduction studied in this paper are the rate of air injection, the porous medium area (area of air injection), and the bubble diameter. To obtain the optimum conditions for robustness, various flow speeds and measured positions of local shear stress are regarded as indicative factors. The numbers of levels for the controllable and the indicative factors are set to 3 and 2, respectively. The value of parameters corresponding to levels for the individual controllable factors and indicative factors are presented in Tables I and II, respectively. As shown in Table I, the parameters for the area of air injection are $A=30\times100$, 60×100, and $90\times100\,\text{mm}^2$ for level 1, level 2 and level 3, respectively; three bubble sizes, $d=50$, 100 and 200 μm, are investigated; the rates of air injection are set to $Q_a=20$, 40 and 60 L/min. Referring to Table II, the flow speeds considered in this study are 4 and 6 m/s; the distances from air injection to the measured position of shear stress are set to 150 and 300 mm. The bubble drag reduction in this paper is expressed in terms of the drag ratio (DR) and is defined as follows:

$$\text{DR}=\frac{\tau}{\tau_0} \tag{17}$$

where τ is the local shear stress after the bubbles are injected and τ_0 denotes the corresponding value with no bubbles in the flow. This means that the drag has been reduced by bubbles if DR$<$1. For the problem of drag reduction, DR is the response that this experiment is attempting to minimize.

Based on the number of controllable factors selected and the level number set, this study implements a standard $L_{27}(3^{13})$ orthogonal array in which the superscript represents the maximum

Table I. Factors and corresponding parametric level values.

Parametric value	Factor A (mm^2)	Factor B (μm)	Factor C (L/min)
Level 1	30×100	50	20
Level 2	60×100	100	40
Level 3	90×100	200	60

DOI: 10.1002/fld

Table II. Parametric level values for indicative factors.

Parametric value	Flow speed (m/s)	Measured position (mm)
Level 1	4	150
Level 2	6	300

available number of controllable factors, the number '3' denotes that each controllable factor contains three levels, and the suffix represents the total experiments required. The controllable factors and interactions between each two factors should be arrayed in accordance with a certain rule to reduce the 'confounding error' as much as possible. Refer to Ross [21] for the array setting rule.

4. RESULTS AND DISCUSSION

4.1. Grid independent test

First, the grid-independent test was carried out to ensure that the distribution of grid nodes did not artificially affect the computational outcome. In this study, the distribution of grid nodes is uniform in the streamwise (x-direction) and lateral direction (z-direction); however, along the vertical height of the channel (y-direction), the distribution of nodes is non-uniform. In the y-direction near the upper and lower walls, the gradients of flow properties are so large that the cells near walls must be fine enough to ensure that they obtain the precise shear stress; contrarily, cells far away from the walls are rather coarse in order to reduce computational requirements. Four cases with various distributions of nodes in the y-direction were selected for the grid test. In these cases, the intervals in the x-direction are 1 and 7.5 mm in the z-direction. In the y-direction, varying node quantities were examined: 45 nodes for case I, 65 nodes for case II, 85 nodes for case III, and 105 nodes for case IV. These tests were carried out under the following conditions: flow speed $V=4\,\mathrm{m/s}$, area of air injection $A=30\times100\,\mathrm{mm}^2$, bubble diameter $d=200\,\mu\mathrm{m}$, and rate of air injection $Q_\mathrm{a}=20\,\mathrm{L/min}$. The shear stresses for every case are listed in Table III; the values in the last row of the table represent the percentage of difference between each two case results. Table III reveals that for case I, in which only 45 nodes are in the y-direction, the cells seem too coarse near the walls to capture the large magnitude of the flow gradient and the shear stress is, therefore, underestimated ($5.378\,\mathrm{N/m}^2$). As the number of nodes increases, the cells become finer and the shear stresses increase, e.g. $8.295\,\mathrm{N/m}^2$ for case II, $9.033\,\mathrm{N/m}^2$ for case III and $9.147\,\mathrm{N/m}^2$ for case IV. Comparing the results of case III and IV, the percentage of difference is only 1.25%. The shear stresses for each case are also presented in Figure 2, in which the ordinate indicates the shear stress and the abscissa represents the total number of cells in the computational domain. As shown in Figure 2, initially an apparent difference in results exists between cases I and II. As the number of cells increases, the curve in the figure asymptotes to a horizontal line, implying that the differences in results become smaller as the number of cells increases. Finally, the results for cases III and IV are very close, indicating that the cells of case III are fine enough to accurately evaluate the wall-shear stress, and that finer cells only have a limited effect upon the result. In order to minimize computational time, the number of nodes in the y-direction was, therefore, set to 85 for all computations in later studies.

DOI: 10.1002/fld

Table III. Shear stresses for test cases.

Test case	Case I	Case II	Case III	Case IV
Shear stress (N/m^2)	5.378	8.295	9.033	9.147
Percentage (%)	35.17	8.17	1.25	

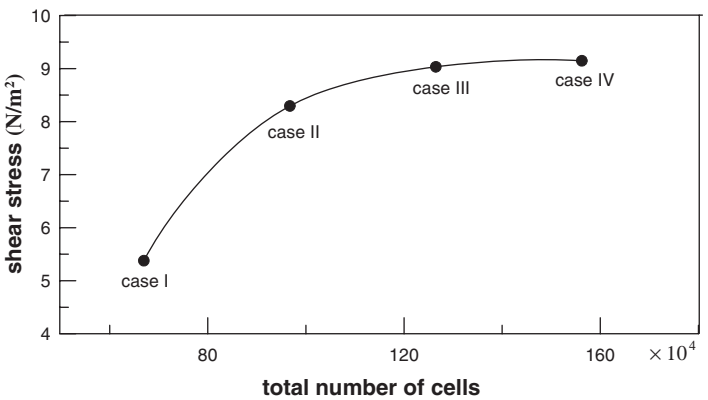

Figure 2. Grid-independent test: the number of nodes in the y-direction is 45 for case I, 65 for case II, 85 for case III and 105 for case IV (measured at 150 mm from the rear edge of the porous plate).

4.2. Numerical results and robust parameters

Based on the conditions planned in the $L_{27}(3^{13})$ orthogonal array (left half of Table IV), the numerical simulations were carried out under various flow speeds (4 and 6 m/s) and the shear stresses were obtained at different measured positions (150 and 300 mm). The Arabic numbers in the left half of Table IV represent the parametric level of controllable factors and the parameter values corresponding to each level for an individual controllable factor can be referenced from Table I. In this orthogonal array, the area of air injected is expressed as factor A and the bubble diameter and the rate of air injection are marked as factor B and factor C, respectively. $A \times B$ represents the interaction between factor A and factor B; the symbol e can be regarded as an experimental error. Based on the computational results, the average DR and the signal-to-noise (S/N) ratio were derived and are listed in the right half of Table IV. The original data are provided in Appendix A. As shown in Table IV, the average DR is 0.166 and the average S/N ratio is 15.725. This efficiency of drag reduction (83.4%) is comparable in magnitude to the microbubble drag reduction experiment conducted by Madavan *et al.* [7]. Additionally, for case 21 in Table IV, where $A = 90 \times 100\,mm^2$, $d = 50\,\mu m$ and $Q_a = 60\,L/min$, the minimum DR (0.115) and the maximum S/N ratio (18.731) can be obtained.

Table V shows the effect of the factorial parametric level on the DR and the S/N ratio; it represents the effect of level variance on the response. Table V(a) is the effect on the DR. It shows that the variance in the level of factor C (the rate of air injection) has the most significant influence on the DR. In the other words, factor C is the most significant factor related to drag reduction. In

DOI: 10.1002/fld

Table IV. $L_{27}(3^{13})$ orthogonal array and the corresponding results.

Level	A	B	A×B	A×B	C	A×C	A×C	B×C	*e*	*e*	B×C	*e*	*e*	Ave. DR	S/N
1	1	1	1	1	1	1	1	1	1	1	1	1	1	0.213	13.364
2	1	1	1	1	2	2	2	2	2	2	2	2	2	0.177	14.954
3	1	1	1	1	3	3	3	3	3	3	3	3	3	0.122	18.153
4	1	2	2	2	1	1	1	2	2	2	3	3	3	0.206	13.637
5	1	2	2	2	2	2	2	3	3	3	1	1	1	0.172	15.224
6	1	2	2	2	3	3	3	1	1	1	2	2	2	0.123	18.107
7	1	3	3	3	1	1	1	3	3	3	2	2	2	0.201	13.876
8	1	3	3	3	2	2	2	1	1	1	3	3	3	0.171	15.261
9	1	3	3	3	3	3	3	2	2	2	1	1	1	0.126	17.918
10	2	1	2	3	1	2	3	1	2	3	1	2	3	0.216	13.247
11	2	1	2	3	2	3	1	2	3	1	2	3	1	0.178	14.881
12	2	1	2	3	3	1	2	3	1	2	3	1	2	0.119	18.375
13	2	2	3	1	1	2	3	2	3	1	3	1	2	0.206	13.659
14	2	2	3	1	2	3	1	3	1	2	1	2	3	0.173	15.135
15	2	2	3	1	3	1	2	1	2	3	2	3	1	0.119	18.383
16	2	3	1	2	1	2	3	3	1	2	2	3	1	0.203	13.770
17	2	3	1	2	2	3	1	1	2	3	3	1	2	0.147	16.325
18	2	3	1	2	3	1	2	2	3	1	1	2	3	0.123	18.067
19	3	1	3	2	1	3	2	1	3	2	1	3	2	0.214	13.275
20	3	1	3	2	2	1	3	2	1	3	2	1	3	0.174	15.123
21	3	1	3	2	3	2	1	3	2	1	3	2	1	0.115	18.731
22	3	2	1	3	1	3	2	2	1	3	3	2	1	0.202	13.788
23	3	2	1	3	2	1	3	3	2	1	1	3	2	0.169	15.362
24	3	2	1	3	3	2	1	1	3	2	2	1	3	0.116	18.630
25	3	3	2	1	1	3	2	3	2	1	2	1	3	0.199	13.895
26	3	3	2	1	2	1	3	1	3	2	3	2	1	0.171	15.256
27	3	3	2	1	3	2	1	2	1	3	1	3	2	0.121	18.213
													Ave.	0.166	15.725

contrast, the level of factor A (the area of air injection) is the least significant among these main factors and its influence upon the DR is almost deemed to be an error. For the effect of factor interaction, the table shows that the interaction of factor B and factor C (B × C) has a significant influence on the DR. However, the influence of the interaction of other factors on the DR can be regarded as being negligible. Table V(b) lists the effect of parametric level on the S/N ratio. By comparing Table V(b) with (a), it can be observed that the effect of parametric level on the DR and the S/N ratio has the same patterns. To analyze the results of experiments involving multiple factors, the use of the S/N ratio over standard analysis (use of the average of results) is preferred, because it provides guidance for the selection of the optimum parametric level based on the least variation around the target and on the average value closed to the target [22]. Table V(b) shows that if factor A (the area of air injection) is set to level 3, the S/N ratio is the maximum (15.808); similarly, if factor B (the bubble diameter) and factor C (the rate of air injection) are set to level 3, maximum S/N ratios of 15.843 and 18.286 are achieved. By comparing Table V(b) with (a), it can be observed that the parametric levels, which are determined by the maximum S/N ratio in Table V(b), can be used to obtain the minimum DR in Table V(a). It is noteworthy that the influence exercised by the interaction of factor B and factor C (B × C) on both the DR and the

DOI: 10.1002/fld

Table V. Effect of factorial level on drag ratio and S/N ratio.

	A	B	A×B	A×B	C	A×C	A×C	B×C	*e*	*e*	B×C	*e*	*e*
(a) *Effect on drag ratio*													
Level 1	0.168	0.170	0.164	0.167	0.207	0.166	0.163	0.165	0.167	0.166	0.170	0.163	0.166
Level 2	0.165	0.165	0.167	0.164	0.170	0.166	0.166	0.168	0.164	0.167	0.166	0.167	0.164
Level 3	0.164	0.162	0.166	0.166	0.120	0.165	0.168	0.168	0.167	0.164	0.162	0.167	0.167
Level effect	0.003	0.007	0.004	0.003	0.086	0.001	0.004	0.003	0.003	0.004	0.008	0.004	0.003
Rank	9	3	7	11	1	13	4	12	8	6	2	5	10
(b) *Effect on S/N ratio*													
Level 1	15.610	15.566	15.824	15.668	13.613	15.716	15.865	15.761	15.682	15.702	15.534	15.835	15.701
Level 2	15.760	15.769	15.648	15.806	15.280	15.743	15.691	15.582	15.827	15.661	15.736	15.684	15.794
Level 3	15.808	15.843	15.706	15.704	18.286	15.720	15.622	15.835	15.669	15.815	15.909	15.660	15.683
Level effect	0.197	0.276	0.176	0.138	4.673	0.026	0.243	0.253	0.158	0.153	0.375	0.175	0.111
Rank	6	3	7	11	1	13	5	4	9	10	2	8	12

DOI: 10.1002/fld

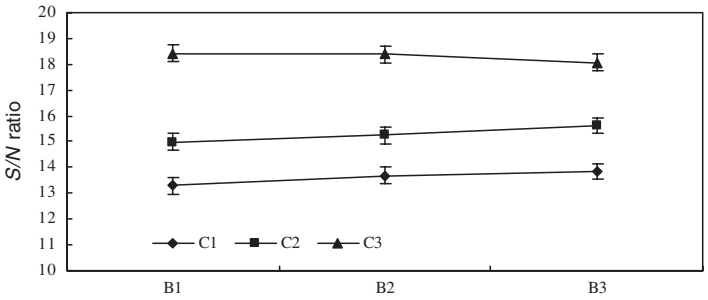

Figure 3. The interaction of factor B and C affecting on the S/N ratio.

S/N ratio is significant, meaning that a nonlinear relationship exists between these two factors, which is sufficient to influence the response. Consequently, in order to assign the factorial level for each factor, these two factors should be taken into consideration together, not individually. The interaction of factor B and factor C upon the S/N ratio is presented in Figure 3, in which the symbol of B1 represents that the factorial level of factor B is 1. Other symbols are similarly assigned. From Figure 3, it is obvious that the condition B1 C3 offers the maximum S/N ratio; hence, for factor B, level 1 should be chosen, not level 3 as shown in Table V. Summarily, with the consideration of the external environmental variances, the composite level of A3 B1 C3 possesses the optimum robust characteristic, which corresponds with the conclusion reached through case 21 in Table IV.

4.3. Contribution of factors

ANOVA is used to examine the contribution of each controllable factor and the interactions between factors. Table VI presents the ANOVA results for the DR and S/N ratio, where the symbol SS is the sum of the squares, DOF indicates the degrees of freedom, MS (mean square) is the sum of square divided by the degrees of freedom, F represents the 'F test' and ρ_c is the contribution to drag reduction. The F test is a certification used to examine the influence of factorial level variance on responses. When the value of the F test for a factor is large, it implies that this factor's level variance effect on the response is important, compared with the variance due to the experimental error, i.e. the factor is significant. In addition, the error term in the table covers the total of unsolved and unknown factorial variances and some variances arising from experiment errors. Hence, the effects of experimental errors marked e in Table IV are taken into the error term. In the ANOVA of the DR, this study also pays special attention to the flow speed, which is regarded as an indicative factor, in order to realize the influence flow speed has on bubble drag reduction. The ANOVA of the DR is discussed first. In the preliminary stage (not presented in this paper), the analysis reveals that the value of F test for factor A is less than $F_{0.1}$, meaning that as the 90% confidence level is a criterion employed to certify the factors; factor A fails to pass the certification. It implies that compared with other factors, the effect factor A exercises on the DR is low and it is quite possible that this low a variance might be caused by experimental error; hence, the variance of factor A should be pooled to the error term. A similar situation also occurred with the factorial interaction A × B and A × C. The pooled data are entered as dashes in Table VI. However, the pooled MS that have small values are still presented in parentheses in the table for comparison. Referring to Table VI(a), it can be observed that factor C possesses the

DOI: 10.1002/fld

Table VI. ANOVA for drag ratio and S/N ratio.

Factor	SS	DOF	MS	F	$F_{0.1}$	ρ_c (%)
(a) *ANOVA of drag ratio*						
A	(0.00023)	(2)	(0.00012)	—	—	—
B	0.00095	2	0.00048	3.5097	2.35755	0.35
C	0.13441	2	0.06721	496.225	2.35755	69.87
A × B	(0.00040)	(4)	(0.00010)	—	—	—
A × C	(0.00040)	(4)	(0.00010)	—	—	—
B × C	0.00118	4	0.00029	2.17178	2.00312	0.33
Flow speed	0.04217	1	0.04217	311.3797	2.75743	21.90
Error	0.01327	98	0.00014			7.55
Total	0.19199	107				100.00
(b) *ANOVA of S/N ratio*						
A	(0.19083)	(2)	(0.09542)	—	—	—
B	0.36864	2	0.18432	2.78169	2.62395	0.23
C	100.962	2	50.48080	761.8376	2.62395	97.46
A × B	(0.23598)	(4)	(0.05900)	—	—	—
A × C	(0.28655)	(4)	(0.07164)	—	—	—
B × C	0.93741	4	0.23435	3.53675	2.28577	0.65
Error	1.19271	18	0.06626			1.67
Total	103.4604	26				100.00

maximum contribution to the DR (69.87%). Factor B has been qualified at a 90% confidence level, but the contribution is as low as 0.35%. Furthermore, the contribution of B × C is 0.33%, but it is able to pass certification at the 90% confidence level, meaning that even though the interaction is low, it is sufficient to affect the response. These analytical outcomes agree with the conclusions discussed in Table V. Additionally, Table VI(a) reveals that the flow speed is the factor that has the second highest contribution to the drag reduction and its contribution is as high as 21.90%. Combining the results of Table VI(a) with the data listed in Table IV, under the configuration of optimum parametrical levels (A3 B1 C3), the prediction for the DR can be obtained by the following equation:

$$(y)_{\mathrm{DR,pred.}} = \overline{y}_{\mathrm{DR}} + (\overline{\mathrm{B1}}_{\mathrm{DR}} - \overline{y}_{\mathrm{DR}}) + (\overline{\mathrm{C3}}_{\mathrm{DR}} - \overline{y}_{\mathrm{DR}}) + [(\overline{\mathrm{B1C3}}_{\mathrm{DR}} - \overline{y}_{\mathrm{DR}}) - (\overline{\mathrm{B1}}_{\mathrm{DR}} - \overline{y}_{\mathrm{DR}}) - (\overline{\mathrm{C3}}_{\mathrm{DR}} - \overline{y}_{\mathrm{DR}})] = 0.119 \tag{18}$$

where $\overline{y}_{\mathrm{DR}}$ is average DR, the variable $\overline{\mathrm{B1}}_{\mathrm{DR}}$ represents the average of the DR obtained when the level of factor B is 1, and other variables are defined analogically. The predicted value of the DR obtained by solving Equation (18) is greater than the outcome of case 21 in Table IV (0.115) due to the fact that when Equation (18) is employed to estimate the value, factor A is deemed to be an experimental error and its effect is not included in the formulation.

Table VI(b) is the ANOVA of the S/N ratio. As mentioned above, when a factor has an F test value less than $F_{0.1}$, the effect of this factor is pooled into the error terms. It is notable that since the flow speed is not a controllable factor, it is not included in this analysis. As shown in Table VI(b), the influence on the S/N ratio imposed by factors and the factorial interactions present the same trend as Table VI(a) indicates. Factor C has the greatest influence on the S/N ratio and

DOI: 10.1002/fld

its contribution is 97.46%. The predicted value of the S/N ratio is as follows:

$$(y)_{\mathrm{S/N,pred.}} = \overline{y}_{\mathrm{S/N}} + (\overline{\mathrm{B1}}_{\mathrm{S/N}} - \overline{y}_{\mathrm{S/N}}) + (\overline{\mathrm{C3}}_{\mathrm{S/N}} - \overline{y}_{\mathrm{S/N}}) + [(\overline{\mathrm{B1C3}}_{\mathrm{S/N}} - \overline{y}_{\mathrm{S/N}}) - (\overline{\mathrm{B1}}_{\mathrm{S/N}} - \overline{y}_{\mathrm{S/N}}) - (\overline{\mathrm{C3}}_{\mathrm{S/N}} - \overline{y}_{\mathrm{S/N}})] = 18.418 \quad (19)$$

where the $\overline{y}_{\mathrm{S/N}}$ is the average S/N ratio. The predicated S/N ratio is a little lower than the S/N ratio obtained by case 21 in Table IV (18.731).

Student's distribution [22] is adopted in this study to calculate the confidence intervals (CI); the CI of predictions can be obtained by the following formula:

$$\mathrm{CI} = t_{\alpha/2}(f_{\mathrm{E}}) \times \frac{S}{\sqrt{m_{\mathrm{e}}}} \quad (20)$$

where α is the significance level, f_{E} is the degree of freedom of the error term, S is standard deviation, and m_{e} is the effective sample size. When $\alpha = 0.05$ is adopted, i.e. under the 95% confidence level, the confidence interval calculated using Equation (20) is 0.0067 and 0.3122 for the DR and S/N ratio, respectively. The effective sample size m_{e} in (20) is defined as

$$m_{\mathrm{e}} = \frac{\text{number of total experiment data}}{\text{total degrees of freedom in the equation of the predicted value}} \quad (21)$$

To summarize, when the factorial parametric levels are at the optimum configuration (A3 B1 C3), the largest area of air injection $A = 90 \times 100\,\mathrm{mm}^2$, the smallest bubble diameter $d = 50\,\mu\mathrm{m}$ and the maximum rate air injection $Q_{\mathrm{a}} = 60\,\mathrm{L/min}$, under the 95% confidence level, the predicted DR is 0.119 ± 0.0067, and the S/N ratio is 18.418 ± 0.3122.

4.4. Confirmation

On principle, the prediction obtained by the Taguchi method should be compared with confirmation experiments, which were carried out under the condition of optimum configuration, to examine the reliability of prediction. However, all data investigated in this work were obtained numerically; therefore, there is a lack of substantial data obtained from the experiments. In addition, repeating numerical simulations deemed as confirmation experiments has no meaning, because these results will be the same. Hence, the evaluation of the robustness, instead of the reliability, was adopted in this paper to evaluate the prediction. The analysis of Table VI(a) reveals that the flow speed, which is regarded as environmental noise, contributes greatly to the drag reduction. Hence, the simulations were carried out under the extended range of the flow speed, and then the computational results were compared with the prediction to assess the robustness of quality. Under the configuration of optimum parametrical levels, the DRs obtained as the flow speeds of $V = 3$–$7\,\mathrm{m/s}$ are listed in Appendix B. Based on the results in Appendix B, the distribution of the probability density for the S/N ratio is shown in Figure 4 and compared against the distribution of probability density of the prediction. Referring to Figure 4, it can be seen that the majority of the confidence interval areas for the predicted and the numerical results overlap. This indicates that the optimum configuration has included the significant factors and determined the most appropriate parametric levels; hence, the response can overcome the variance from the operating condition, implying that the configuration of parametric levels possesses ensuring the robustness of quality; that is to say, the prediction obtained by the Taguchi method may be popularized to get a robust design.

DOI: 10.1002/fld

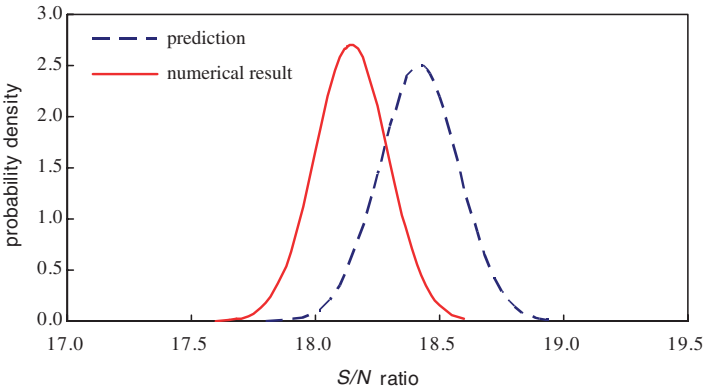

Figure 4. Distributions of probability density of the S/N ratio for the prediction and the numerical results.

4.5. Characteristic of drag reduction

The characteristic curves of drag reduction are presented in Figure 5 to investigate the relationships between the drag reduction and the void fraction, C_V, defined as

$$C_V = \frac{Q_a}{Q_a + Q_w} \tag{22}$$

where Q_w and Q_a are the liquid flow rate and air flow rate, respectively. In Figure 5, the DRs, measured at 150 mm from the air injection, are represented by solid lines and the dashed lines indicate the DRs measured at 300 mm. Substantial past researches have regarded the void fraction as an important parameter related to drag reduction and concluded that the efficiency of drag reduction increases as C_V increases. Figure 5(a) represents the characteristic curves for the optimum parametric level, A3 B1. For comparison, the characteristic curves for an entirely different configuration, A1 B3, indicating a small area of air injection and large bubbles, are presented in Figure 5(b). As shown in Figure 5(a) and (b), the DRs decrease as C_V increases. Additionally, it is clear that better efficiencies of drag reductions can be reached at a high flow speed ($V = 6$ m/s). Referring to Figure 5(a), the DRs measured at 150 and 300 mm from the air injection are almost the same values at $V = 4$ m/s. When $V = 6$ m/s, a small decline in drag reduction at a measured position of 300 mm is observed, as C_V is very small. On the other hand, Figure 5(b) shows that under the condition of A1 B3, the efficiencies of drag reductions do not strongly persist unless C_V is large.

Under the condition of the optimum parametric level (A3 B1 C3), the magnification of the volumetric fraction of bubbles distributed in channel for the flow speed at 4 m/s is presented in Figure 6. The color scale displayed on the left of Figure 6 indicates the magnitude of the bubble volumetric fraction. As shown in the figure, the volumetric fraction of bubbles very close to the upper wall is almost equal to one and drops suddenly just away from the wall. This phenomenon suggests that the bubbles injected into the channel form a film of gas–liquid mixture that covers the upper wall, and leads to frictional resistance being reduced. All the distributions of bubbles in the channel for the other study cases (not presented in this paper) are the same as the result of A3 B1 C3. This may be the reason why there is minimal contribution of the bubble size factor to drag reduction in this study; because the bubbles that were injected were too crowded together and

DOI: 10.1002/fld

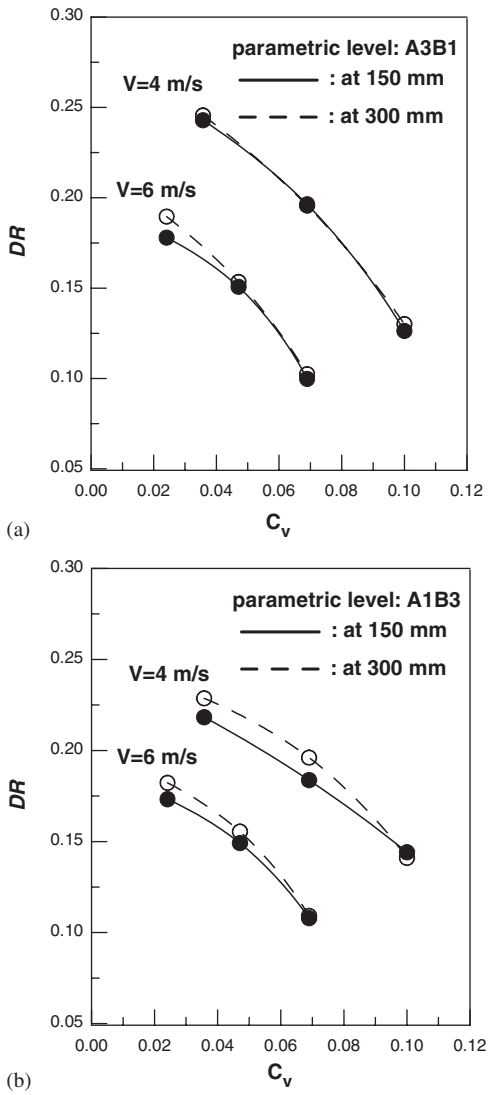

Figure 5. Effect of air void ratio on drag ratio: (a) characteristic curves for optimum levels (A3B1) and (b) characteristic curves for the configuration of A1B3.

formed a mixture film. The enlargement of the location for injection of air bubbles is shown in Figure 7; the velocity vectors of the mixture flow have been combined with the volume fractions of air in a water channel for convenient discussion. Under the upper wall, the x-component of the velocity within a mixture film is larger than the mean velocity of water in the channel. The reason for this phenomenon is that air bubbles injected through a porous medium gather close to the upper wall (due to the effect of buoyancy) to mix with the water; thus, leading to increased velocity of the mixture flow and rate of volume flow locally. In the region close to the upper wall, the volume

DOI: 10.1002/fld

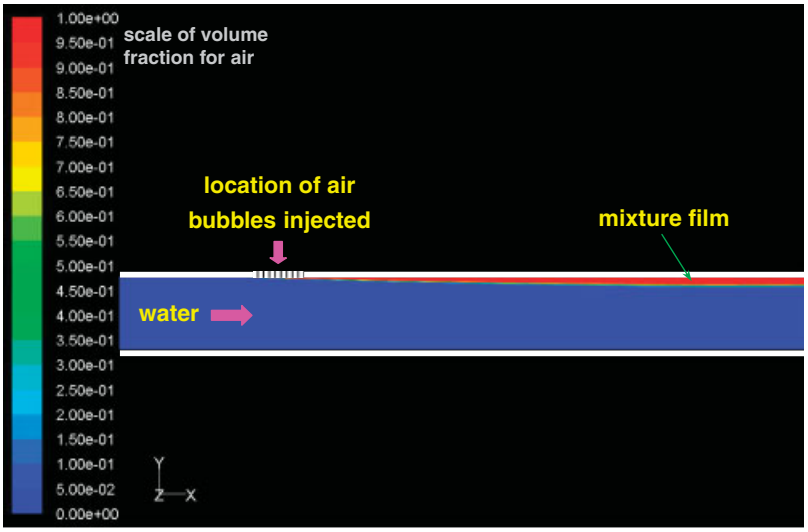

Figure 6. The distribution of volume fraction of air bubbles in channel ($V = 4\,\mathrm{m/s}$).

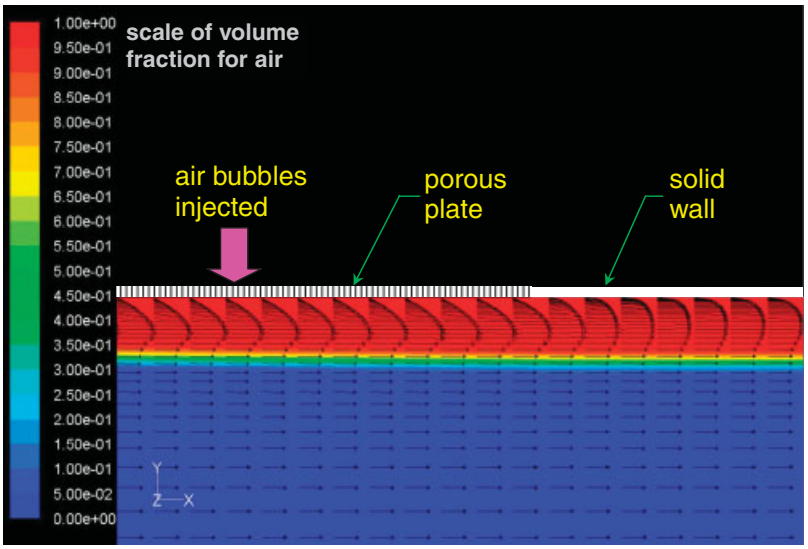

Figure 7. The velocity vectors of mixture flow and the volume fractions of air in water channel (the enlargement of the location of injecting air bubbles).

fraction for mixed water with air bubbles is present. The volume fraction of air ranges from 0.9 to 1.0, in contrast to that of the water, which ranges from 0.0 to 0.1. This mixing region is known as the mixture film, in which the volume fraction of air is dominant. Hence, the decreasing molecular viscosity μ and density ρ is very evident in the mixture film. For fully developed turbulent channel flow, the total shear stress is equal to the summation of both the viscous and turbulent shear stress,

DOI: 10.1002/fld

where the viscous shear stress is proportional to the molecular viscosity and the mean velocity gradient, and the turbulent shear stress (Reynolds stress) depends on the density and turbulent fluctuations. Therefore, in the region very close to the upper wall the viscous shear is reduced, due to the decreasing molecular viscosity and/or the mean velocity gradient (such as under the porous plate in which the air bubbles is injected). Simultaneously, in the mixture film, the turbulent shear stress is also reduced due to the effect of a lower density and possible suppression of the turbulent fluctuations. As a result, the total shear stress close to the upper wall is effectively decreased in the mixture film. The air/mixture film usually provides higher efficiency of drag reduction than that by microbubbles; the difficulty in maintenance of an air/mixture film is a disadvantage to the application. However, in a bounded field, e.g. channel flow, an air/mixture film is easy to maintain so that the effect of drag reduction is quite evident to the upper wall.

Furthermore, the effect of drag reduction between the present computation and the experimental data conducted by Murai *et al.* [12] was compared. That experiment was concerned with the mechanism of drag reduction using large air bubbles within turbulent channel flow, in which the bubble sizes were approximately between 2 and 90 mm. The test section was a horizontal rectangular channel of height 10 mm, width 100 mm, and length 6000 mm. The air injection device was a porous plate with an injection area $A = 14 \times 48\,\text{mm}^2$. The mean liquid flow speeds in the channel range from 1 to 2 m/s. Drag reduction and its persistence were investigated by measuring the local wall-shear stresses at 250, 1000, and 4000 mm downstream of the air injection. However, for appropriate comparison, only the experimental measurements at the 250 mm location, with a flow speed of 2 m/s, were adopted. The present computational results were obtained at a distance of 300 mm from the air injection. In addition, the non-dimensional Reynolds number $Re_h = V D_h/v$ was introduced, where D_h represents the hydraulic diameter. Because the size of the test section differs between the present computational simulations and the previous experiment, the use of the Reynolds number can eliminate the discrepancy in the size of the test section. To ensure consistency of the Reynolds number, several new simulations were carried out under the condition $V = 1.333$ m/s. Table VII shows the simulation conditions for various C_v and also the relationship between C_v and Q_a. First, simulations were carried out at the optimum parametric levels, i.e. $A = 90 \times 100\,\text{mm}^2$ and $d = 50\,\mu\text{m}$. In addition, as the bubble sizes in the experiment are 2 mm at minimum, the simulation results as $d = 2000\,\mu\text{m}$ were also provided in the comparison. Figure 8 shows the effect of drag reduction upon the simulation and the experiment data as $Re_h = 3.62 \times 10^4$. In the figure, the dotted line is the experimental result and the two solid lines represent the computations. The solid lines represent the conditions $d = 50\,\mu\text{m}$ and $d = 2000\,\mu\text{m}$. As shown in Figure 8, a negative correlation between the DR and the void fraction occurs for all results. For the experimental result, the effect of drag reduction is not obvious until the void fraction exceeds approximately 0.12, and the maximum drag reduction of 55% is reached as $C_v = 0.26$. Alternatively, for the computations, drag is reduced immediately, even when the void fraction is small. The maximum drag reductions are 70.6 and 61.0% for $d = 50$ and $2000\,\mu\text{m}$, respectively. As shown in Figure 8 by the computational results, better drag reduction efficiency can be obtained if the bubble size is small. This fact agrees with the analytical results shown in Figure 3. However,

Table VII. Simulation conditions ($A = 90 \times 100\,\text{mm}^2$ and $V = 1.333$ m/s).

C_v	0.05	0.10	0.15	0.20	0.25
Q_a (L/min)	9.47	20.00	31.76	44.99	59.99

DOI: 10.1002/fld

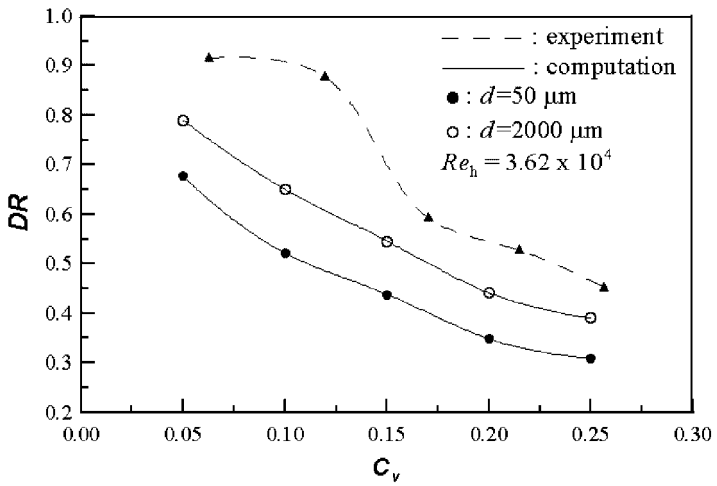

Figure 8. Comparison of the drag reduction between the computations and the experimental data presented by Murai *et al.* [12].

the DR for the computation appears comparatively small when compared with the experimental results, even though the bubble size is consistent across both the computation and the experiment. The authors suggest that the larger DR obtained in the experiment occurs due to the small air injection area. The small air injection area used in the experiment implies that the air bubbles are injected into the flow at high velocity. It is likely that air bubbles injected at an excessive velocity destroy the turbulent boundary layer, and as a result reduce the effect of drag reduction.

5. CONCLUSION

This study utilizes the Taguchi method to develop a set of optimum robust parametric levels for air bubble drag reduction in turbulent channel flow. While the flow speed and measured position of local shear stress were considered as indicative factors, the area of air injection, bubble size, and the rate of air injection were investigated as controllable factors. The L_{27} (3^{13}) orthogonal array was used to design the experimental conditions, and then the turbulent flows with bubbles were simulated by FLUENT. The standard k–ε turbulent model was adopted to resolve the turbulent flow, and the Mixture model served as a multi-phase model in this paper. The distribution of bubbles in the channel has been shown. It can be observed that the bubbles in the channel form as a thin mixture film and cover the upper wall to reduce the frictional resistance. The local shear stress on the upper wall of the channel was obtained to examine the efficiency of drag reduction. Results indicate that, under the scope of the parametric values set in this paper, the minimum drag ratio (DR) 0.115 can be reached, when the largest area and maximum rate of air injection, and the smallest bubble diameter are adopted. Via ANOVA, factorial contribution analysis reveals that the rate of air injection is the most significant factor for robustness. In addition, it can be observed that the flow speed also has an important influence on bubble drag reduction, implying that, as the bubble technique is implemented to reduce the resistance, the vessel speed is crucial. These conclusions are consistent with other published studies. Under the optimum configuration

DOI: 10.1002/fld

of parametric levels, additional simulations were carried out at the extended range of $V = 3$–$7\,\mathrm{m/s}$ with results indicating that the optimum parametric levels determined by the Taguchi method possess great robustness of quality. On the condition of $Re_h = 3.62 \times 10^4$, simulation results using the bubble sizes $d = 50$ and $2000\,\mu\mathrm{m}$ were compared with the experimental data presented by Murai *et al.* The DRs of the computations are comparatively small compared with the experiment data. The comparison result also shows that better drag reduction can be obtained if bubble size is small.

APPENDIX A

Original data.

	$V = 4\,\mathrm{m/s}$		$V = 6\,\mathrm{m/s}$	
DR	$d_1 = 150\,\mathrm{mm}$	$d_2 = 300\,\mathrm{mm}$	$d_1 = 150\,\mathrm{mm}$	$d_2 = 300\,\mathrm{mm}$
1	0.234	0.243	0.186	0.189
2	0.194	0.204	0.153	0.157
3	0.140	0.138	0.105	0.106
4	0.225	0.236	0.177	0.187
5	0.190	0.192	0.150	0.156
6	0.136	0.140	0.108	0.109
7	0.218	0.229	0.173	0.182
8	0.184	0.196	0.149	0.155
9	0.144	0.141	0.108	0.109
10	0.239	0.243	0.185	0.194
11	0.200	0.206	0.152	0.154
12	0.133	0.137	0.102	0.104
13	0.227	0.233	0.180	0.183
14	0.191	0.198	0.151	0.153
15	0.134	0.136	0.102	0.104
16	0.221	0.228	0.178	0.186
17	0.091	0.193	0.148	0.155
18	0.138	0.142	0.106	0.108
19	0.243	0.246	0.178	0.190
20	0.196	0.194	0.151	0.153
21	0.122	0.134	0.100	0.102
22	0.227	0.230	0.169	0.181
23	0.192	0.187	0.147	0.150
24	0.122	0.134	0.102	0.106
25	0.223	0.231	0.161	0.181
26	0.188	0.196	0.149	0.151
27	0.136	0.142	0.102	0.103
Ave.	0.181	0.190	0.143	0.149
	0.186		0.146	

DOI: 10.1002/fld

APPENDIX B

The numerical results under the conditions of $A = 90 \times 100\,\text{mm}^2$, $d = 50\,\mu\text{m}$, and $Q_\text{a} = 60\,\text{L/min}$: the DR_1 and DR_2 are the drag ratios measured at 150 and 300 mm from the porous medium, respectively, are given.

$V = 3\,\text{m/s}$		$V = 5\,\text{m/s}$		$V = 7\,\text{m/s}$	
DR_1	DR_2	DR_1	DR_2	DR_1	DR_2
0.152	0.155	0.116	0.118	0.095	0.096

NOMENCLATURE

A	area of air injection, mm^2
$\mathbf{a}$	acceleration of the bubble, m/s^2
CI	confidence interval
C_v	void fraction, $C_v = Q_\text{a}/(Q_\text{a} + Q_\text{w})$
c_k	mass fraction for phase k, $c_k = \alpha_k \rho_k / \rho_\text{m}$
DOF	degree of freedom
DR	drag ratio, $DR = \tau/\tau_0$
d	diameter of bubble, m
F	F test
$\mathbf{F}$	body force, nt
f_drag	drag function
f_E	degree of freedom of error
$\mathbf{g}$	gravitational acceleration, m/s^2
H	vertical height of the test section, m
I	unit tensor
k	turbulent kinetic energy per unit mass, J/kg
MS	mean square
m_e	effective sample size
p	static pressure, nt/m^2
Q_a	airflow rate, L/min
Q_w	liquid flow rate, L/min
Re	relative Reynolds number, $Re = \rho_q \lvert\mathbf{V}_p - \mathbf{V}_q\rvert d/\mu_q$
Re_h	Reynolds number based on the hydraulic diameter
S	standard deviation
S/N	signal to noise ratio, dB
SS	sum of the square
V	flow speed, m/s
$\mathbf{V}$	velocity vector, m/s
$\mathbf{V}_{\text{dr},k}$	drift velocity of phase k, m/s
$\mathbf{V}_k$	velocity vector of phase k, m/s

DOI: 10.1002/fld

$\mathbf{V}_{\mathrm{m}}$	velocity vector of the mixture flow, m/s
$\mathbf{V}_{pq}$	relative velocity of the dispersed phase (p) related to the primary phase (q), m/s
x	coordinate in the streamwise direction
y	coordinate in the vertical direction of the test section
$(y)_{\mathrm{DR,pred}}$	prediction for the drag ratio
$\overline{y}_{\mathrm{DR}}$	average drag ratio
$(y)_{\mathrm{S/N,pred}}$	prediction for the S/N ratio, dB
$\overline{y}_{\mathrm{S/N}}$	average S/N ratio, dB
z	coordinate in the lateral direction of the test section
α	significant level
α_k	volume fraction of phase k
ε	turbulent dissipation rate, $\mathrm{m}^2/\mathrm{s}^3$
ρ	density, $\mathrm{kg/m}^3$
ρ_c	factorial contribution
ρ_{m}	density of mixture, $\mathrm{kg/m}^3$
ρ_k	density of phase k, $\mathrm{kg/m}^3$
μ	molecular viscous coefficient, Pas
μ_{m}	dynamic viscous coefficient of the mixture, kg/ms
τ	local shear stress, Pa
τ_0	local shear stress with no bubbles in the flow, $\mathrm{nt/m}^2$
τ_{p}	particle relaxation time, s
$\overline{\tau}$	stress tensor

REFERENCES

1. McCormic ME, Bhattacharyya R. Drag reduction of a submersible hull by electrolysis. *Naval Engineers Journal* 1973; **85**:11–16.
2. Kitagawa A, Sugiyama K, Ashihara M, Hishida K, Kodama Y. Measurement of turbulence modification by microbubbles causing frictional drag reduction. *4th ASME JSME Joint Fluids Engineering Conference*, Honolulu, HI, 2003. *Paper No. FEDSM2003-45648*.
3. Dubnishchev YN, Evseev AR, Sobolev VS, Utkin EN. Study of gas-saturated turbulent streams using a Doppler velocimeter. *Journal of Applied Mechanical Technology Physics* 1975; **16**(1):114–119.
4. Merkle CL, Deutsch S. Drag reduction. In *Frontiers in Experimental Fluid Mechanics*, Gad-el-Hak M (ed.). Lecture Notes in Engineering, vol. 46. Springer: Berlin, 1986; 291–335.
5. Kato H, Iwashina T, Miyanaga M, Yamaguchi H. Effect of microbubbles on the structure of turbulence in a turbulent boundary layer. *Journal of Marine Science and Technology* 1999; **4**:155–162.
6. Kawamura T, Fujiwara A, Takahashi T, Kato H, Matsumoto Y, Kodama Y. The effects of the bubble size on the bubble dispersion and skin friction reduction. *Proceeding of the 5th Symposium on Smart Control of Turbulence*, Tokyo, 2004; 145–151.
7. Madavan NK, Deutsch S, Merkle CL. Reduction of turbulent skin friction by microbubbles. *Physical Fluids* 1984; **27**:356–363.
8. Tsai J-F, Chen C-C. Experimental study on the micro-bubble drag reduction effect in water tunnel and towing tank. *The 13th Asia-Pacific Workshop on Marine Hydrodynamics*, Shanghai, China, 2006.
9. Latorre R. Ship hull drag reduction using bottom air injection. *Ocean Engineering* 1997; **24**(2):161–175.
10. Kato H, Kodama Y. *Microbubbles as a Skin Friction Reduction Device—A Midterm Review of the Research*. National Maritime Research Institute, 2001.
11. Latorre R, Miller A, Phillips R. Micro-bubble resistance reduction on a model SES catamaran. *Ocean Engineering* 2003; **30**:2297–2309.
12. Murai Y, Fukuda H, Oishi Y, Kodama Y, Yamamoto F. Skin friction reduction by large air bubbles in a horizontal channel flow. *International Journal of Multiphase Flow* 2007; **33**:147–163.

DOI: 10.1002/fld

13. Kawamura T, Kodama Y. Direction numerical simulation of wall turbulence with bubbles. *Proceedings of the 2nd Symposium on Smart Control of Turbulence*, 2001; 135–143. Available from: http://www.nmri.go.jp/turbulence/pdf/symposium/FY2000/Kawamura.pdf.
14. Kawamura T, Kodama Y. Numerical simulation method to resolve interactions between bubbles and turbulence. *International Journal of Heat and Fluid Flow* 2002; **23**:627–638.
15. Sugiyama K, Kawamura T, Takagi S, Matsumoto Y. Numerical simulation on drag reduction mechanism by microbubbles. *Proceeding of 3rd Symposium on Smart Control of Turbulence*, 2002; 129–138. Available from: http://www.nmri.go.jp/turbulence/pdf/symposium/FY2001/Sugiyama.pdf.
16. Drew DA. Mathematical modeling of two-phase flow. *Annual Review of Fluid Mechanics* 1983; **15**:261–291.
17. Murai Y, Matsumoto Y. Numerical simulation of turbulent bubbly plumes using Eulerinan–Lagrangian bubbly flow modeling equation. *Proceeding of ASME FED*, vol. FED236, 1996; 67–74.
18. Legner HH. A simple model for gas bubble drag reduction. *Physical Fluids* 1984; **27**:2788–2790.
19. Madavan NK, Merkle CL, Deutsch S. Numerical investigations into the mechanisms of microbubble drag reduction. *Journal of Fluids Engineering* 1985; **107**:370–377.
20. Marie JL. A simple analytical formulation for microbubble drag reduction. *Physical Chemical Hydrodynamics* 1986; **8**:213–220.
21. Ross PJ. *Taguchi Techniques for Quality Engineering*. McGraw-Hill: New York, 1996.
22. Roy RK. *A Primer on the Taguchi Method*. Van Nostrand Reinhold: New York, 1990.
23. Kim DK, Choi DW, Choa Y-H, Kim HT. Optimization of parameters for the synthesis of zinc oxide nanoparticles by Taguchi robust design method. *Colloids and Surface A*: *Physicochemical Engineering* 2007; **331**:170–173.
24. Nikbakht R, Sadrzadeh M, Mohammadi T. Effect of operating parameters on concentration of citric acid using electrodialysis. *Journal of Food Engineering* 2007; **83**:596–604.
25. Fluent Inc. *Fluent 6.1 User's Guide*. Fluent Inc.: Lebanon, 2003.
26. Versteeg HK, Malalasekera W. *An Introduction to Computational Fluid Dynamics*; *The Finite Volume Method*. Longman: New York, 1995.

DOI: 10.1002/fld